Formation of vacancies and metallic-like domains in photochromic rare-earth oxyhydride thin films studied by in-situ illumination positron annihilation spectroscopy

Wu, Ziying; De Krom, Tom; Colombi, Giorgio; Chaykina, Diana; Van Hattem, Gijs; Schut, Henk; Dickmann, Marcel; Brück, Ekkes; Dam, Bernard; Eijt, Stephan W.H.

DOI
10.1103/PhysRevMaterials.6.065201

Publication date
2022

Document Version
Final published version

Published in
Physical Review Materials

Formation of vacancies and metallic-like domains in photochromic rare-earth oxyhydride thin films studied by *in-situ* illumination positron annihilation spectroscopy

Ziying Wu [1,*] Tom de Krom [1] Giorgio Colombi [2] Diana Chaykina [1,2] Gijs van Hattem,[1] Henk Schut [3] Marcel Dickmann,[4] Werner Egger,[4] Christoph Hugenschmidt [5] Ekkes Brück [1] Bernard Dam [2] and Stephan W. H. Eijt [1]

[1]*Fundamental Aspects of Materials and Energy, Department of Radiation Science and Technology, Faculty of Applied Sciences, Delft University of Technology, Mekelweg 15, NL-2629 JB Delft, Netherlands*

[2]*Materials for Energy Conversion and Storage, Department of Chemical Engineering, Faculty of Applied Sciences, Delft University of Technology, Van der Maasweg 9, NL-2629 HZ Delft, Netherlands*

[3]*Neutron and Positron Methods for Materials, Department of Radiation Science and Technology, Faculty of Applied Sciences, Delft University of Technology, Mekelweg 15, NL-2629 JB Delft, Netherlands*

[4]*Institut für Angewandte Physik und Messtechnik, Bundeswehr Universität München, D-85577 Neubiberg, Germany*

[5]*Physics Department and Heinz Maier-Leibnitz Zentrum (MLZ), Technische Universität München, D-85748 Garching, Germany*

(Received 28 January 2022; revised 5 April 2022; accepted 23 May 2022; published 21 June 2022; corrected 29 June 2022)

Rare-earth (RE) oxyhydride thin films show a color-neutral, reversible photochromic effect at ambient conditions. The origin of the photochromism is the topic of current investigations. Here, we investigated the lattice defects, electronic structure, and crystal structure of photochromic YH_xO_y and GdH_xO_y thin films deposited by magnetron sputtering using positron annihilation techniques and x-ray diffraction, in comparison with Y, $YH_{\sim 1.9}$, Y_2O_3, Gd, $GdH_{\sim 1.8}$, and Gd_2O_3 films. Positron annihilation lifetime spectroscopy (PALS) reveals the presence of cation monovacancies in the as-deposited Y and $YH_{\sim 1.9}$ films at concentrations of $\sim 10^{-5}$ per cation. In addition, vacancy clusters and nanopores are found in the as-prepared YH_xO_y and Y_2O_3 films. Doppler broadening positron annihilation spectroscopy (DB-PAS) of the Y- and Gd-based films reflects the transition from a metallic to an insulating nature of the RE metal, metal hydride, semiconducting oxyhydride and insulating oxide films. *In-situ* illumination DB-PAS shows the irreversible formation predominantly of di-vacancies, as PALS showed that cation mono-vacancies are already abundantly present in the as-prepared films. The formation of di-vacancies supports conjectures that H^- (and/or O^{2-}) ions become mobile upon illumination, as these will leave anion vacancies behind, some of which may subsequently cluster with cation vacancies present. In addition, in RE oxyhydride films, partially reversible shifts in the Doppler parameters are observed that correlate with the photochromic effect and point to the formation of metallic domains in the semiconducting films. Two processes are discussed that may explain the formation of these metallic domains and the changes in optical properties associated with the photochromic effect. The first process considers the reversible formation of metallic nanodomains with reduced O : H composition by transport of light-induced mobile hydrogen and local oxygen displacements. The second process considers metallic nanodomains resulting from the trapping of photoexcited electrons in an e_g orbital at the yttrium ions surrounding positively charged hydrogen vacancies that are formed by light-induced removal of hydrogen atoms from octahedral sites. When a sufficiently large concentration, on the order of $\sim$10%, is reached in a certain domain of the film, band formation of the e_g electrons may occur, leading to an Anderson-Mott insulator-metal transition like the case of yttrium trihydride in these domains.

DOI: 10.1103/PhysRevMaterials.6.065201

I. INTRODUCTION

Inorganic photochromic materials have attracted extensive interest because they possess a higher physicochemical stability than organic photochromic materials. They are promising for applications in the fields of energy-saving smart windows [1], adaptive eyewear lenses [2], and sensors [3]. Traditional inorganic photochromic materials include transition metal oxides and doped metal halides, e.g., tungsten oxide [4] and copper-doped silver halide [5]. The photochromism of yttrium oxyhydride thin films (YH_xO_y), where oxygen is incorporated into YH_{2-x} metal hydride films by *ex-situ* oxidation, was first reported in 2011 [6]. Other rare-earth (RE) metal oxyhydride films, based on Gd, Er, Dy, and Sc, also showed similar photochromic properties, characterized by a strong reduction in the optical transmission below the bandgap energy in a broad wavelength range in the visible and near-infrared (IR) upon ultraviolet (UV) illumination [7,8]. These photochromic oxyhydride films were prepared by reactive magnetron sputtering of metal dihydride films in an argon/hydrogen atmosphere above a specific critical deposition pressure followed by exposure to air. The incorporation of oxygen into the RE metal hydride films during postoxidation does not induce a phase transition, but the crystal lattice expands and maintains a

*Corresponding author: Z.Wu-2@tudelft.nl

face-centered cubic (fcc)-like structure similar to the dihydride films [7]. The bandgap, optical properties, and electrical properties of oxyhydride films can be modified by tailoring the chemical composition (O^{2-} and H^- contents) by varying the deposition pressure [8–12].

However, the mechanism of photochromism in RE oxyhydride films is still unclarified. The photochromic mechanism of the well-known inorganic photochromic material Cu-doped AgCl is associated with the formation of metallic silver clusters due to the light-induced electron generation and transport that induces a change in the valence state of Ag ions according to $Ag^+ + e^- \rightarrow Ag^0$ [13]. The Ag^0 atoms move to interstitial sites and cluster to form metallic regions, leading to pronounced photodarkening of the material. A similar mechanism may be involved in RE oxyhydride films. Based on spectroscopic ellipsometry, Montero *et al.* [14] proposed that the photodarkening of YH_xO_y films is related to the formation of metallic domains since the optical transmittance of YH_xO_y under illumination could be modeled well by the formation of a small fraction of up to 6 vol. % of metallic domains. The domains were supposed to be YH_2-like, but it remained unclear how they formed. Based on solid-state nuclear magnetic resonance (NMR), Chandran *et al.* [15] showed that a rearrangement of mobile hydrogen species occurs during illumination of YH_xO_y, which reverses during bleaching, correlating with the photochromic changes. Our previous positron annihilation studies [8,16] showed that UV illumination induces the formation of vacancies, providing additional (indirect) support for ion mobility during photodarkening. In that study, the formation of vacancies appeared irreversible during the subsequent bleaching phase, suggesting that the vacancies observed by positron annihilation are not directly responsible for the photochromic effect.

In this paper, we further clarify the formation of vacancies during photodarkening. Moreover, we monitored the changes in electronic structure during illumination and subsequent bleaching and found that these are (at least partially) reversible in character. Positron annihilation lifetime spectroscopy (PALS) was used to identify the sizes of vacancy-like defects and concentrations of vacancies in as-prepared $Y/YH_{\sim 1.9}/YH_xO_y/Y_2O_3$ films. X-ray diffraction (XRD) and Doppler broadening positron annihilation spectroscopy (DB-PAS) were employed to investigate the crystal structure and electronic structure via detection of electronic momentum distributions of as-deposited Gd- and Y-based films. In addition, *in-situ* illumination DB-PAS was used to probe the evolution of vacancies and electronic structure properties of the oxyhydride films during UV illumination and subsequent bleaching in the dark. We describe and discuss two different possible mechanisms for the photodarkening of the RE metal oxyhydride films consistent with the reversible changes observed in the *in-situ* illumination positron studies. The first mechanism involves the formation of H-rich domains that exhibit a metallic-like electronic structure, enabled by photoinduced transport of hydrogen. Modeling based on diffusion-limited positron trapping in such H-rich domains suggests that the characteristic sizes of these domains are in the range of ∼1–20 nm. The second mechanism involves the formation of positively charged hydrogen vacancies at octahedral sites with a localized charge-compensating electron in an e_g-state orbital at the surrounding yttrium ions. At sufficiently high concentrations, overlap between the e_g-state orbitals of these localized electrons may occur, leading to band formation and a local metallic behavior in the respective domains in the YH_xO_y film, like what has been proposed for the Anderson-Mott insulator-to-metal transition of yttrium trihydride at a composition of $YH_{\sim 2.7}$.

II. EXPERIMENT

A. Sample preparation

The RE metal dihydride and oxyhydride films were deposited on unheated UV-grade fused silica (f-SiO_2) substrates by reactive direct current (DC) magnetron sputtering of yttrium or gadolinium targets (with 99.9% purity) in an Ar/H_2 gas mixture. The DC power supplied to the Y and Gd target was 200 and 180 W, respectively. The sputtered metal dihydride films were deposited under a pressure of 0.3 Pa, while the oxyhydride films were obtained from the postoxidation of metal dihydride films deposited above the critical pressure of ∼0.4 Pa for YH_xO_y and 0.6 Pa for GdH_xO_y films [7], at room temperature. A second type of RE metal dihydride films was prepared by posthydrogenation of sputtered Y or Gd films capped with a thin Pd layer. The Pd layer not only protects the film from oxidation but also catalyzes the hydrogenation process [17]. Some of the oxyhydride films were capped by a thin aluminum (Al) layer after exposure of the reactively sputtered dihydride films to air for ∼3 h. The Al layer was used to prevent interaction of the oxyhydride films with the ambient (or vacuum) environment during the experiments. The Y and Gd metal films were deposited in an argon atmosphere under a pressure of 0.3 Pa, while the Y_2O_3 and Gd_2O_3 metal oxide films were made in an Ar/O_2 atmosphere under a pressure of 0.3 Pa via pulsed DC reactive magnetron sputtering. Detailed information about the deposition method can be found in Ref. [8]. All the samples used are listed in Tables I and SI in the Supplemental Material [18].

B. Characterization

Grazing-incidence XRD measurements were performed on a PANalytical X-pert Pro diffractometer with a Cu $K\alpha$ source ($\lambda = 1.54$ Å) at room temperature, and the angle of incidence was fixed at $\omega = 2^\circ$ for all measurements. The XRD patterns were analyzed by the Rietveld refinement method using the FULLPROF suite [19,20]. The crystal structures of the various films deduced from the Rietveld refinement are in agreement with previous findings [8,9], with a hexagonal close-packed (hcp) structure and space group of $P6_3/mmc$ for the Y and Gd films, and a fcc structure and space group $Fm\text{-}\bar{3}m$ for the RE metal dihydride and oxyhydride thin films. Yttrium oxide (Y_2O_3) crystallizes in a body-centered-cubic structure with space group $I\text{-}a\bar{3}$ [21]. Detailed information on the Rietveld refinement analysis of the films, including the crystal structures, lattice parameters, and volume per Y (or Gd) atom, is given in the Supplemental Material [18].

PALS studies were performed using the pulsed low-energy positron lifetime spectrometer (PLEPS) of the neutron-induced positron source (NEPOMUC) facility at the Heinz

TABLE I. List of main samples, deposition pressures, and experiments.

Samples	Deposition pressure	Measurements
Y	0.3 Pa	PALS, DB-PAS, XRD
$YH_{\sim 1.9}$//Pd	0.3 Pa (hydrogenation)	PALS, DB-PAS, XRD
YH_xO_y-1	0.5 Pa	PALS, DB-PAS, XRD, *in-situ* illumination DB-PAS
YH_xO_y-2	0.5 Pa	PALS
YH_xO_y//Al	0.5 Pa	DB-PAS, XRD, *in-situ* illumination DB-PAS
Y_2O_3	0.3 Pa	PALS, DB-PAS
Gd	0.3 Pa	DB-PAS
$GdH_{\sim 1.8}$//Pd	0.3 Pa (hydrogenation)	DB-PAS, XRD
GdH_2	0.3 Pa	DB-PAS, XRD
GdH_xO_y	0.8 Pa	DB-PAS, XRD
GdH_xO_y//Al	0.8 Pa	DB-PAS, XRD
GdH_xO_y	0.9 Pa	DB-PAS, XRD, *in-situ* illumination DB-PAS
GdH_xO_y//Al	0.9 Pa	DB-PAS, XRD, *in-situ* illumination DB-PAS
Gd_2O_3	0.3 Pa	DB-PAS

Maier-Leibnitz Zentrum (MLZ) research reactor in Garching [22–24]. For each lifetime spectrum, 4×10^6 counts were collected. The instrument time resolution function, determined by PALS measurements on a reference *p*-doped SiC sample at each positron implantation energy, was considered when decomposing the experimental PALS spectra. The extracted time resolution was ∼180 ps. The lifetime spectra of eight samples, collected at various positron implantation energies in the range of 0.5–16 keV, were fitted by the POSWIN program [25,26].

DB-PAS was employed to study the electronic structure and vacancy-type defects in Y- and Gd-based thin films. DB-PAS depth profiles of the films were measured at room temperature with positron implantation energies ranging from 0.1 to 20 keV, using the variable energy positron beam facility at the Reactor Institute Delft [27]. A high-purity Ge (HPGe) detector cooled by liquid nitrogen with the energy resolution of 1.2 keV was used to detect the energy distribution of the ∼511 keV γ rays produced by the annihilation of positrons and electrons. The intensity of the low-energy positron beam at the sample position is $\sim 10^4\, e^+/s$, and the full width at half maximum of the beam diameter is ∼8 mm. The depth profiles of the extracted shape (S) and wing (W) parameters were fitted by the VEPFIT program [28]. The S parameter represents positron annihilation with valence electrons, which provides sensitivity to the electronic structure and open volume defects such as vacancies or vacancy clusters, while the W parameter reflects positron annihilation with (semi-)core electrons, which provides information on the local chemical environment of the positron trapping site. Momentum windows of $|p| < 3.0 \times 10^{-3}\, m_0c$ and $8.2 \times 10^{-3}\, m_0c < |p| < 23.4 \times 10^{-3}\, m_0c$ were used for determining the S and W parameters, respectively.

Optical transmittance measurements were performed in a custom-built setup equipped with a white source (DH-2000BAL, Ocean Optics) and a silicon charge-coupled device array spectrometer (HR4000, Ocean Optics). The light source triggering the photochromic effect of oxyhydride films used in the transmittance measurements was a narrow wavelength LED (385 nm, $I \sim 75\,mW/cm^2$). In the *in-situ* illumination DB-PAS experiments, the same LED equipped with a Köhler lens system is placed ∼45 cm behind the sample, with an intensity of $\sim 33\,mW/cm^2$ at the position of the sample.

III. RESULTS AND DISCUSSION

A. Open-volume defects in Y-based thin films examined by PALS

To examine the nature of the positron annihilation sites and presence of vacancy-related defects in the as-deposited films, PALS experiments were performed on various yttrium-based films. This PALS study enabled us to probe the sizes and concentrations of vacancy-related defects in the films. Representative spectra obtained for the $YH_{\sim 1.9}$//Pd and YH_xO_y-1 films, collected at a positron implantation energy of 4 keV are shown in Fig. 1, together with best fits obtained using POSWIN analysis. To reliably extract the lifetime parameters for each film, we considered the PALS spectra collected at 3 and 4 keV since, at these positron implantation energies, the largest fraction of positrons (∼91–96% for $YH_{\sim 1.9}$//Pd and ∼94–98% for YH_xO_y-1) annihilate inside the film, according to VEPFIT analysis [28], as presented in Fig. S3 in the Supplemental Material [18]. The positron lifetime spectra of all Y-based thin films at 3 and 4 keV are shown in Fig. S4 in the Supplemental Material [18]. The spectra of the metallic Y and YH_{2-x} films decay according to a sum of exponential decay components to close to the background level beyond ∼6 ns. In contrast, a component with a long exponential decay is observed in the PALS spectra of YH_xO_y and Y_2O_3 films. This shows that orthopositronium (o-Ps) pick-off annihilation is present in the YH_xO_y and Y_2O_3 films, while it is absent in the metallic Y and YH_{2-x} films. Positronium (Ps) is a hydrogen-like bound state of a positron and an electron. Orthopositronium (o-Ps) has spin $S = 1$ and a long self-annihilation lifetime in vacuum of ∼142 ns due to annihilation into 3 γ-ray photons and can be formed in sufficient large open space, for instance, nanopores present in a material. The self-annihilation lifetime of ∼142 ns can be reduced substantially by so-called pick-off annihilation, in which the positron of o-Ps annihilates with an electron of

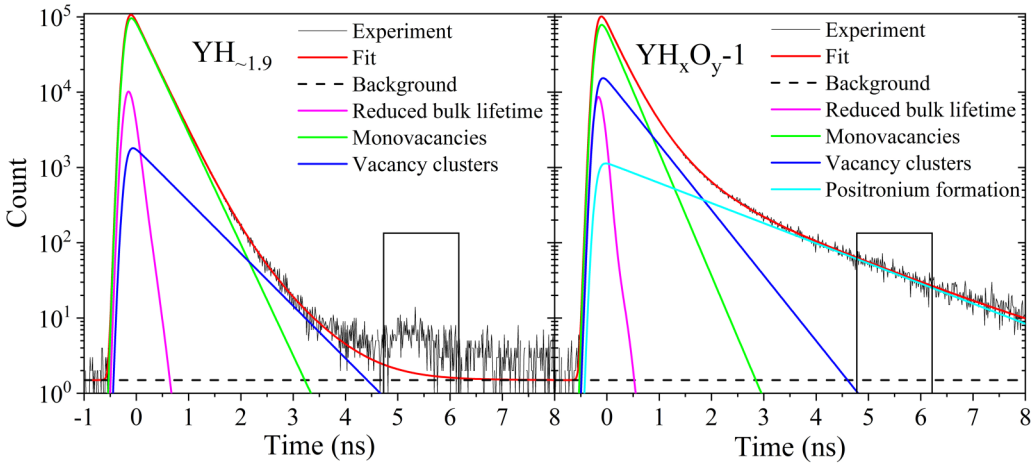

FIG. 1. PALS spectra collected at a positron implantation energy of 4 keV of (a) $YH_{\sim 1.9}$//Pd with three-component best-fit analysis and (b) YH_xO_y-1 with four-component best-fit analysis using the POSWIN program. The peaks in the rectangular region in the spectra are excluded in the analysis since they correspond to backscattered positrons that annihilate at a different location in the sample chamber of the pulsed low-energy positron lifetime spectrometer (PLEPS).

opposite spin of the surrounding material under emission of 2 γ quanta. The formation of o-Ps in the YH_xO_y and Y_2O_3 films therefore indicates the presence of nanopores. However, o-Ps formation is likely inhibited in the metal and metal hydride films due to their metallic character.

The PALS spectra of the Y and YH_{2-x} films were satisfactorily fitted by a three-lifetime-component analysis, while the spectra of YH_xO_y and Y_2O_3 films were satisfactorily fitted by a four-lifetime-component analysis using the POSWIN analysis program [25,26]. For all Y-based films, the lifetime of the first component extracted in the analysis (Tables II and SIII in the Supplemental Material [18]) is significantly shorter than typical values for the positron bulk lifetime characteristic for annihilation in defect-free materials [29]. We attribute this first component to positron annihilation in a defect-free local environment in our vacancy-containing films, which only occurs at short timescales before these positrons had the chance to find and trap into vacancy-related point defects in the films. The lifetime of the first component is reduced with respect to the positron bulk lifetime by the competitive process of positron trapping in vacancy-related open volume defects, which provides additional decay channels that add to the decay rate of the first component [29]. The other two lifetime components, which are linked to positron annihilation in open volume defects, have lifetimes that are characteristic for the size of the vacancy-related defect, vacancy cluster, or nanopore involved, while their intensity is associated with the concentration of the respective open volume defect. As we will discuss further on, the second component with observed positron lifetimes in the range of 260–295 ps is related to positron trapping in monovacancies, while the third component with a lifetime τ_3 in the range of 500–700 ps may originate from larger vacancy clusters. The fourth component seen for YH_xO_y and Y_2O_3 films with long lifetimes in the range of 1.5–3.2 ns corresponds to pick-off annihilation of o-Ps formed in nanopores in the films. The best-fit parameters of lifetimes (τ_i), intensities (I_i), and average lifetimes (τ_{av}) of all Y-based films at 4 and 3 keV are presented in Tables II and SIII in the Supplemental Material [18], respectively.

1. Two-defect positron trapping model

To elucidate the size and concentration of the vacancy-related defects, a two-defect positron trapping model [29] was applied to extract the bulk lifetime (τ_b), positron trapping rate (k_i), and defect concentrations (C_i) of all samples. In the two-defect positron trapping model, we consider that positrons may be trapped and annihilate in two different types of vacancy-related defects independently. We neglect detrapping of positrons from either of the vacancy-related traps. Additionally, positrons may annihilate in defect-free regions of the material (bulk annihilation) if they do not get trapped in either type of defect before annihilation. According to this model, the lifetime of the first component τ_1 corresponds the reduced bulk lifetime, which satisfies $\frac{1}{\tau_1} = \frac{1}{\tau_b} + k_1 + k_2$, with

TABLE II. Positron lifetimes (τ_i), intensities (I_i), and average lifetimes (τ_{av}) for the PALS spectra of Y-based thin films collected at 4 keV as deduced from POSWIN best-fit analysis.

Samples	τ_1 (ps)	τ_2 (ps)	τ_3 (ps)	τ_4 (ns)	I_1 (%)	I_2 (%)	I_3 (%)	I_4 (%)	τ_{av} (ps)
Y	65 ± 3	279 ± 1	683 ± 22	–	6 ± 0.2	92 ± 0.2	1.5 ± 0.2	–	272 ± 1
$YH_{\sim 1.9}$//Pd	73 ± 5	294 ± 1	624 ± 17	–	5 ± 0.2	92 ± 0.2	3 ± 0.3	–	293 ± 3
YH_xO_y-1	47 ± 5	266 ± 4	500 ± 20	1.63 ± 0.03	3.8 ± 0.2	71 ± 2	22 ± 2	4.2 ± 0.2	365 ± 17
YH_xO_y-2	60 ± 4	281 ± 3	638 ± 29	2.16 ± 0.05	5.2 ± 0.3	78 ± 1	13 ± 1	4.2 ± 0.2	395 ± 9
Y_2O_3	58 ± 5	276 ± 4	539 ± 16	3.03 ± 0.06	5.1 ± 0.3	71 ± 2	21 ± 2	3.4 ± 0.1	412 ± 13

TABLE III. Positron bulk lifetime τ_b, positron trapping rates k_i ($i = 1, 2$), and defect concentrations C_i ($i = 1, 2$) for Y-based thin films obtained from the average of the respective values extracted from PALS spectra collected at 3 and 4 keV. The error ranges correspond to the standard deviations.

Samples	τ_b (ps)	$k_1(10^{10}\,s^{-1})$	$k_2(10^{10}\,s^{-1})$	C_1 (10^{-6})	C_2 (10^{-6})
Y	235 ± 4	1.0 ± 0.1	0.02 ± 0.001	10 ± 1	<0.1
$YH_{\sim 1.9}$//Pd	260 ± 6	0.8 ± 0.1	0.03 ± 0.003	8 ± 1	<0.1
YH_xO_y-1	238 ± 6	1.5 ± 0.3	0.5 ± 0.1	15 ± 3	1 ± 0.5
YH_xO_y-2	242 ± 4	1.2 ± 0.2	0.33 ± 0.05	12 ± 2	0.4 ± 0.2
Y_2O_3	256 ± 4	0.9 ± 0.1	0.27 ± 0.03	9 ± 1	0.3 ± 0.1

k_1 and k_2 being the trapping rates in the two types of defects. As will be explained further on, the second component τ_2 for the series of films studied here is a signature of cation monovacancies, and τ_3 is a signature of vacancy clusters. The minor contributions from the long lifetime o-Ps components (<5%) in the lifetime spectra of YH_xO_y and Y_2O_3 were ignored when using this two-defect positron trapping model. The intensities of the other three components were rescaled accordingly to ensure $\sum_{i=1}^{3} I_i = 1$, as required for application of the two-defect positron trapping model. The main equations of this model:

$$k_1 = \mu C_1 = I_2\left(\frac{1}{\tau_1} - \frac{1}{\tau_2}\right), \quad (1)$$

$$k_2 = \mu C_2 = I_3\left(\frac{1}{\tau_1} - \frac{1}{\tau_3}\right), \quad (2)$$

$$\tau_b = \left(\frac{I_1}{\tau_1} + \frac{I_2}{\tau_2} + \frac{I_3}{\tau_3}\right)^{-1}, \quad (3)$$

are used to derive the positron trapping rates k_1 and k_2 in the two types of defects and the positron bulk lifetime τ_b from the lifetimes τ_i and intensities I_i ($i = 1, 2, 3$) extracted from the positron lifetime spectra. The trapping coefficient μ for single vacancies in solids is generally on the order of $10^{15}\,s^{-1}$ [29,30]. Since empirical or theoretical values for the trapping coefficients for defects in the Y-based films are not available, we set $\mu = 10^{15}\,s^{-1}$ for monovacancies in our analysis. The trapping coefficient will be approximately proportional to the number of vacancies n for small vacancy clusters V_n ($n \leqslant 5$), according to the equation $\mu_n = n\mu$, while it will saturate at a high value for larger vacancy clusters since the trapping coefficient will be limited by the positron mobility [29]. Correspondingly, we included a multiplication factor of 5 in the estimation of the trapping coefficient for V_5 clusters and a factor of 7–8 for V_{10} clusters [29]. The τ_b, k_i, and C_i for Y-based thin films determined from the average of the respective values as extracted at 3 and 4 keV are shown in Table III. The expressions used to derive the standard deviations in these parameters are given in the Supplemental Material [18].

The extracted bulk lifetime for the hcp Y thin film of 235 ± 4 ps is comparable with previous studies that report an experimental bulk lifetime of 249 ps and a calculated bulk lifetime of 215 ps for hcp Y [31], indicating that the two-defect trapping model is valid for the Y thin film. The dominant second component, with an intensity ∼92%, has a lifetime of 279 ps which is ∼19% larger than the positron bulk lifetime in hcp Y. Such an increase in lifetime is comparable with the case of V_{Mg} monovacancies in Mg, where Mg crystallizes in an hcp structure with the same space group ($P6_3/mmc$) as Y. The positron lifetime related to the Mg monovacancies was ∼13% larger than the positron bulk lifetime in defect-free Mg [32,33]. This suggests that the second component for the Y film can be attributed to yttrium monovacancies (V_Y). Since the increase of ∼19% is, on the other hand, significantly lower than for Mg divacancies in hcp Mg (with a positron lifetime that is 39% larger than the positron bulk lifetime) [32,33], Y divacancies are not present in the film at detectable concentrations. The concentration of cation monovacancies extracted from the two-defect trapping model is $\sim 10 \times 10^{-6}$ (Table III), which means that 1 out of $\sim 10^5$ Y sites is vacant in the as-deposited Y film. The observed third lifetime component with a lifetime $\tau_3 \sim 680$ ps is a signature of vacancy clusters that are present at a very small amount, while o-Ps formation in the yttrium film is not seen, as can be understood in view of the high density of conduction electrons in the metallic phase that will effectively screen the positron charge, prohibiting Ps formation.

The two-defect trapping model is applied to the $YH_{\sim 1.9}$ and YH_xO_y films as well. The extracted positron bulk lifetime τ_b for the palladium capped $YH_{\sim 1.9}$ ($YH_{\sim 1.9}$//Pd) thin film is ∼260 ps, which is ∼10% larger than that for the hcp Y film. No positron lifetime experiments or calculations on yttrium dihydride nor YH_xO_y are reported in the literature, meaning that no reference values for the positron lifetime in defect-free regions (bulk annihilation) are available. Nevertheless, the observed increase of ∼10% in the extracted positron bulk lifetime for $YH_{\sim 1.9}$ compared with Y can be understood, as it can be attributed to the increase in the lattice volume per Y atom of ∼6% in $YH_{\sim 1.9}$ compared with Y (as extracted from our XRD results presented in Table SII in the Supplemental Material [18]), leading to larger interstitial space, while the concentration of delocalized conduction electrons is also smaller in $YH_{\sim 1.9}$ than Y. Furthermore, the extracted bulk positron lifetime τ_b for $YH_{\sim 1.9}$ is also compatible with the estimated value for the positron bulk lifetime of ∼256 ps based on an empirical equation for the dependence of τ_b on lattice volume for similar metal dihydrides, derived from *ab initio* calculations for defect-free TiH_2 and MgH_2 [33]. The dominant second component with a lifetime τ_2 of ∼294 ps is ∼14% larger than the bulk positron lifetime and can therefore be assigned to V_Y monovacancies with an extracted concentration of $\sim 8 \times 10^{-6}$ (Table III). The low-intensity third lifetime component arises from a very small amount of larger open volume defects such as vacancy clusters, like the case of Y.

Two YH_xO_y thin films, YH_xO_y-1 and YH_xO_y-2, were examined in the positron lifetime measurements. The average extracted bulk lifetime for these films is ∼240 ps. The lifetime of the dominant second component τ_2 for YH_xO_y-1 is ∼11% larger than the bulk positron lifetime τ_b, which again can be attributed to V_Y monovacancies. The concentration of cation vacancies in the as-prepared YH_xO_y films is like those in the Y and YH_2 films. The lifetime of the third component of $\tau_3 \sim 500$ ps is characteristic for vacancy clusters. These vacancy clusters are much more abundant than in the Y and $YH_{\sim 1.9}$ films. The lifetime of $\tau_3 \sim 500$ ps suggests that the number of vacancies in the cluster is >5. Namely, we may compare this value to the positron lifetime ∼450 ps observed for semiconducting GeSn and phosphorus-doped Ge (with bulk lifetimes of ∼225 ps) which is associated with vacancy clusters formed by >5 vacancies [34,35]. Finally, the long lifetime of ∼1.6 ns of the fourth component for YH_xO_y-1 indicates that o-Ps is formed in the oxyhydride films, which may occur in nanopores. The estimated average radius of these nanopores is ∼0.25 nm according to the Tao-Eldrup (TE) model [36,37] which relates the o-Ps pick-off annihilation lifetime to the size of nanopores, assuming that they are spherical in shape. This pore size corresponds to ∼7 atoms missing in 1 u.c. of YH_xO_y (∼V_7 vacancy cluster). We notice that such vacancy clusters with an average size of V_7 could (in principle) also be responsible for the third lifetime component if both positron annihilation as well as Ps formation and annihilation occur in the same type of vacancy clusters. The YH_xO_y-2 film shows similar lifetimes and intensities as YH_xO_y-1, indicating that the dominant second lifetime component of YH_xO_y-2 can also be assigned to V_Y monovacancies, while the fourth lifetime component with τ_4 of ∼2.2 ns indicates the presence of nanopores with an average radius of ∼0.29 nm, corresponding to ∼V_{10} clusters, i.e., somewhat larger than in the YH_xO_y-1 film.

The bulk lifetime of the Y_2O_3 thin film extracted from the two-defect positron trapping model is ∼256 ps, which is a bit larger than the lifetime of 239 ps observed in Y_2O_3 powders [38]. On the other hand, an experimental lifetime of ∼200 ps for sintered Y_2O_3 has also been reported [39], while first-principles calculations using the parameter-free generalized gradient approximation indicate a theoretical bulk lifetime of ∼174 ps [40]. Assuming, nevertheless, that the two-defect positron trapping model is applicable, in this paper, we suggest that V_Y monovacancies are present in the Y_2O_3 film, together with vacancy clusters. The concentrations of these two types of open-volume defects are of the same order as for the YH_xO_y films. Moreover, the presence of a long lifetime component with $\tau_4 \approx 3.0$ ns indicates that o-Ps is formed in nanopores, with an average radius of ∼0.37 nm according to the TE model, assuming a spherical shape. This suggests that ∼14 atoms are locally missing in the lattice (∼V_{14} cluster), showing that the Y_2O_3 film contains larger nanopores than the YH_xO_y films.

Summarizing the results of our PALS spectra study, V_Y cation monovacancies are present in all sputtered films at similar concentrations of the order of 10^{-5}, leading to near-saturation trapping of positrons and a dominant second lifetime component in the PALS spectra. In addition, vacancy clusters are observed in the yttrium oxyhydride and oxide films at a concentration that is ∼15 to 30 times lower than the concentration of the monovacancies. Furthermore, o-Ps pick-off annihilation in the yttrium oxyhydride and oxide films is seen, indicating the presence of nanopores with an average diameter in the range of ∼0.5–0.7 nm. The extracted bulk positron lifetimes for Y, YH_2, and Y_2O_3 are in line with the results of previous studies, supporting the validity of the two-defect positron trapping model used to analyze the PALS results obtained for the magnetron sputtered Y-based thin films. Furthermore, the information extracted by PALS on the vacancies present in the as-prepared yttrium oxyhydride films aids in elucidating the relationship between the changes in DB-PAS parameters observed during illumination and the microstructural changes that cause the photochromic effect (see Sec. III C).

B. Evolution of the electronic structure of Y- and Gd-based thin films observed by DB-PAS

In this section, we describe our investigation of the variation in electronic structure of the Y- and Gd-based thin films, which ranges from metal and semiconductor to insulator behavior, via detection of key aspects of their electron momentum distributions (EMDs) as seen by positrons in DB-PAS. The S and W parameters extracted from VEPFIT analysis of the depth profiles for the Y- and Gd-based metal, metal hydride, oxyhydride, and oxide thin films are presented in the S-W diagrams shown in Fig. 2. A systematic decrease of the S parameter and increase of the W parameter occurs going from the Y or Gd metal to the metal hydride and metal oxide films, which follows the same trend as previously reported for these types of Y-based films in Refs. [8,16] and induced by the variation in their electronic structure [16]. Both Gd and Y metal thin films possess the highest values for the S parameter due to their relatively narrow EMDs, reflecting the contributions of electrons in a free-electron-like conduction band. The incorporation of H into the lattice of Y or Gd leads to a reduction in the S parameter and increase in the W parameter, indicating a broader positron-EMD (PEMD) of the RE dihydride films than the RE films [16]. This is in line with previous positron angular correction of annihilation radiation (ACAR) studies and theoretical models for Y and YH_2 [41,42]. The broadening in part stems from localization of some of the conduction electron states in orbitals associated with H, involving the formation of covalent-ionic Y-H bonds. Detailed insights into the shape of the PEMD and its evolution upon hydrogenation of Y could be obtained by ACAR experiments [43] and/or by *ab initio* calculations [44], which are beyond the scope of this paper. The low S and high W parameters observed for the insulating RE metal oxide films can also be understood, as this is induced by the strongly localized valence electron orbitals centered around the electronegative oxygen atoms, leading to a correspondingly broad PEMD [45,46].

If we now compare the S and W parameters for the Gd, GdH_2, and Gd_2O_3 films with those of the corresponding Y-based films in Fig. 2, very similar trends are observed, while a clear systematic shift toward higher W and lower S parameters is apparent. The higher W parameters of the Gd-based films than the corresponding Y-based films can be attributed to

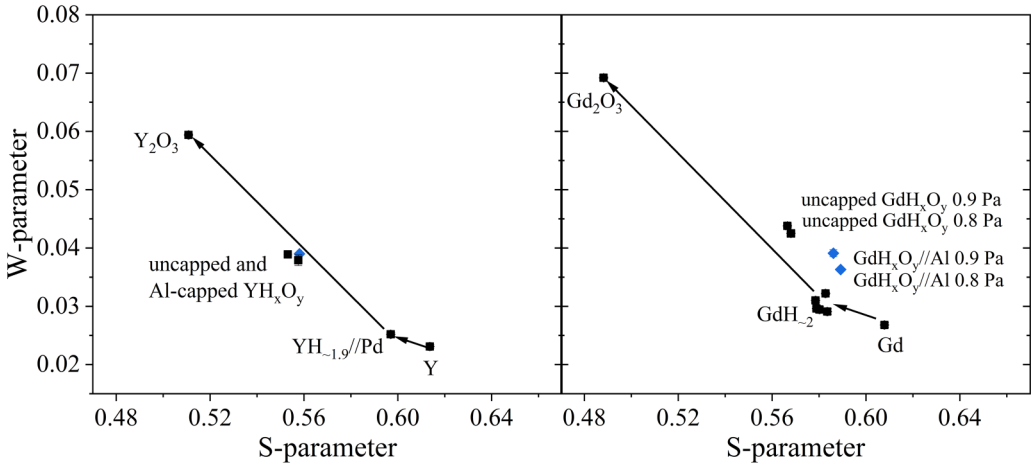

FIG. 2. S-W diagrams of Y- and Gd-based thin films. The Al-capped oxyhydride films are marked with blue color.

electrons in the confined $4f$ orbital of Gd, leading to a broader momentum distribution.

Figure 2 shows that the semiconducting YH_xO_y and GdH_xO_y metal oxyhydride films have S and W parameters that lie in between those of the respective RE metals and RE oxide, reflecting their intermediate composition and ionicity. The S-W points of YH_xO_y films are almost on the line in the S-W diagram connecting Y_2O_3 and $YH_{\sim1.9}$. Clearly, the S-W points of GdH_xO_y films are shifted to higher S values than the line from Gd_2O_3 to GdH_2, suggesting that as-prepared GdH_xO_y films have more and/or larger vacancies that trap positrons than YH_xO_y films. This could be related to a more porous structure of the GdH_xO_y films, as these are deposited at higher pressures (0.8 and 0.9 Pa) than the YH_xO_y films (0.5 Pa).

The S-W points for the uncapped and capped YH_xO_y films (0.5 Pa) are close together and consistent with our previous results [8,16]. The S-W points of the uncapped GdH_xO_y films, on the other hand, are shifted compared with the S-W points of the Al-capped GdH_xO_y films, in the direction toward the S-W point of the Gd_2O_3 film. This suggests that these uncapped GdH_xO_y films have a higher O : H ratio than the Al-capped films, which could be the result of continued incorporation of O into the lattice of the films for prolonged exposure to ambient air. Apparently, in the films investigated in this paper, the air exposure time seems to have a noticeable effect on the oxygen content in GdH_xO_y, while the effect in YH_xO_y is negligible, again pointing to a more porous structure of the GdH_xO_y films.

C. *In-situ* illumination positron Doppler study of the nanostructural evolution of photochromic YH_xO_y and GdH_xO_y films during photodarkening and bleaching

1. Optical properties

The optical transmittance of YH_xO_y and GdH_xO_y films was measured to extract their optical indirect bandgap by Tauc analysis [47], as shown in Fig. S5 in the Supplemental Material [18]. The bandgaps of the three YH_xO_y (0.5 Pa) thin films are similar, with an average bandgap of 2.53 ± 0.08 eV, while the bandgaps for the GdH_xO_y (0.8 Pa) and GdH_xO_y (0.9 Pa) films of 2.36 ± 0.05 eV and 2.51 ± 0.06 eV, respectively, are slightly lower than that for the YH_xO_y films. The increase in bandgap for the GdH_xO_y film deposited at higher pressure is presumably related to the larger degree of oxidation that increases the ionicity of the film, as found in our previous studies [8,9].

The YH_xO_y and GdH_xO_y films show a high transmittance window in the visible and near-IR range (see Fig. S5 in the Supplemental Material [18]). The change of the average optical transmittance in the wavelength range of 450–1000 nm between the virgin and photodarkened states is used to define the photochromic contrast. Figure 3 shows the time dependence of the average transmittance of YH_xO_y and GdH_xO_y films before illumination, during photodarkening and during bleaching, normalized to the transmittance of the as-prepared films. Both YH_xO_y and GdH_xO_y films show a clear reduction in subbandgap transmittance upon UV illumination at 385 nm, i.e., with a photon energy of 3.22 eV, larger than the bandgap. The transmittance of the films nearly fully recovers after stopping illumination and subsequent bleaching for several hours. The change in transmittance nearly saturates after $\sim$1 h illumination for the YH_xO_y (0.5 Pa) and $\sim$0.5 h illumination for the GdH_xO_y (0.8 Pa) sample. The photochromic contrast is $\sim$40% for the YH_xO_y film and $\sim$55% (0.8 Pa) and $>$35% (0.9 Pa) for the GdH_xO_y films.

2. In-situ positron Doppler experiments during UV illumination

In-situ illumination DB-PAS measurements were performed on four oxyhydride film samples, namely, Al-capped YH_xO_y (0.5 Pa), uncapped YH_xO_y (0.5 Pa), Al-capped GdH_xO_y (0.9 Pa), and uncapped GdH_xO_y (0.9 Pa), to investigate the evolution of open-volume defects and electronic structure of the oxyhydride films during photodarkening and subsequent bleaching. To ensure saturation of photodarkening, an illumination time of 2.5 h was used for all oxyhydride films, while the bleaching phase was monitored for $\sim$38 h, i.e., well beyond the time required to achieve full bleaching.

Figure 4 shows the S- and W-parameter depth profiles extracted from the DB-PAS measurements for the four samples before illumination and after full bleaching of the darkened state, respectively. The clear increase in the S parameter and modest reduction in the W parameter indicate that

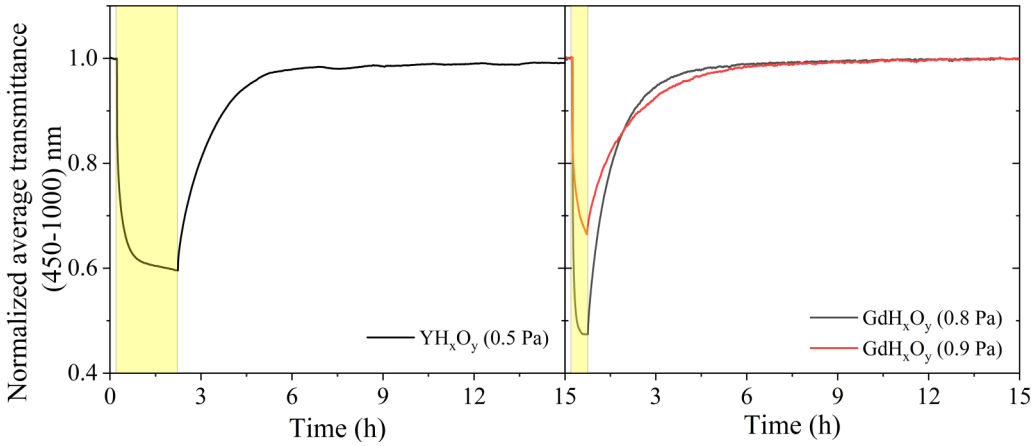

FIG. 3. Normalized transmittance (averaged over the wavelength range of 450–1000 nm) for representative YH_xO_y and GdH_xO_y films during ultraviolet (UV) illumination (yellow regions) at 385 nm, followed by bleaching in the dark.

some of the nanostructural modifications of the oxyhydride films induced by the illumination do not fully recover after bleaching. The changes in the S- and W-depth profiles are qualitatively like those observed in our previous study on Al-capped YH_xO_y films [8], where they were attributed to the formation of V_Y cation vacancies or small vacancy clusters such as V_Y-V_H or V_Y-V_O divacancies, suggesting that some of the H^- and/or O^{2-} ions are removed from their lattice positions during the illumination. More insights are gained by including the results of our current PALS study, which shows that as-prepared YH_xO_y films already contain a large concentration of cation vacancies of $\sim 12 \times 10^{-6}$ to 15×10^{-6} [48] ($I_2 \sim 71$–78%) and vacancy clusters of $\sim 0.4 \times 10^{-6}$ to 1×10^{-6} ($I_3 \sim 13$–22%), leading to near-saturation trapping of positrons in these vacancy-related defects ($I_2 + I_3 \sim 91$–95%) [29,49]. Therefore, we can exclude that the formation of more cation monovacancies plays a dominant role in the observed significant changes in the positron DB S parameter after illumination and bleaching. However, the observed changes may originate from light-induced formation of anion vacancies (V_H, V_O) that are created by H^- or O^{2-} released from their lattice positions. The formed anion vacancies may subsequently cluster with cation monovacancies to form V_Y-V_H or V_Y-V_O divacancies or small vacancy clusters [16], leading to positron trapping and annihilation in these larger vacancy defects. Since the changes in the S and W parameters systematically occur in all films, we infer that, in general, the optical excitation of electron-hole pairs induces the release of H^- or O^{2-} ions from their lattice positions. Such a (possibly local) displacement of

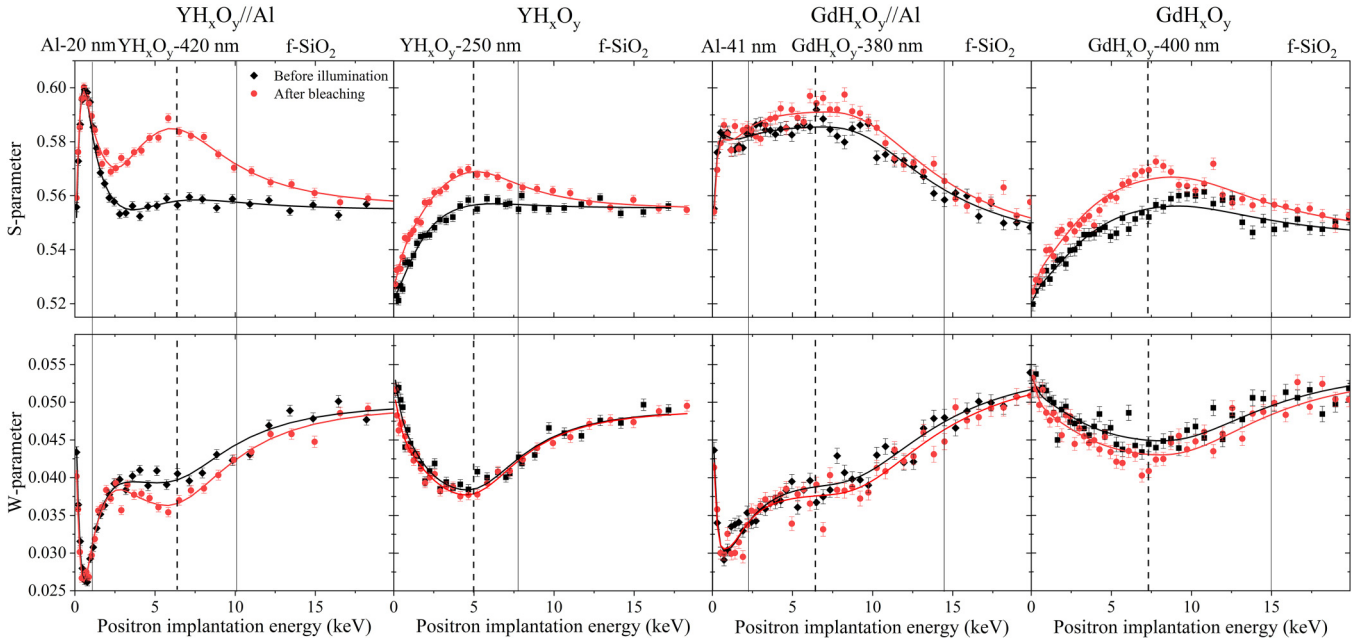

FIG. 4. S- and W-parameter positron Doppler broadening (DB) depth profiles of YH_xO_y//Al (0.5 Pa), YH_xO_y (0.5 Pa), GdH_xO_y//Al (0.9 Pa), and GdH_xO_y (0.9 Pa) thin films before illumination (black symbols and lines) and after 2.5 h illumination and bleaching for ~38 h (red circles and lines). The dashed lines indicate the positron implantation energy for the *in-situ* illumination DB positron annihilation spectroscopy (DB-PAS) measurements shown in Fig. 5. The vertical solid lines indicate the boundaries between adjacent layers based on the VEPFIT analyses.

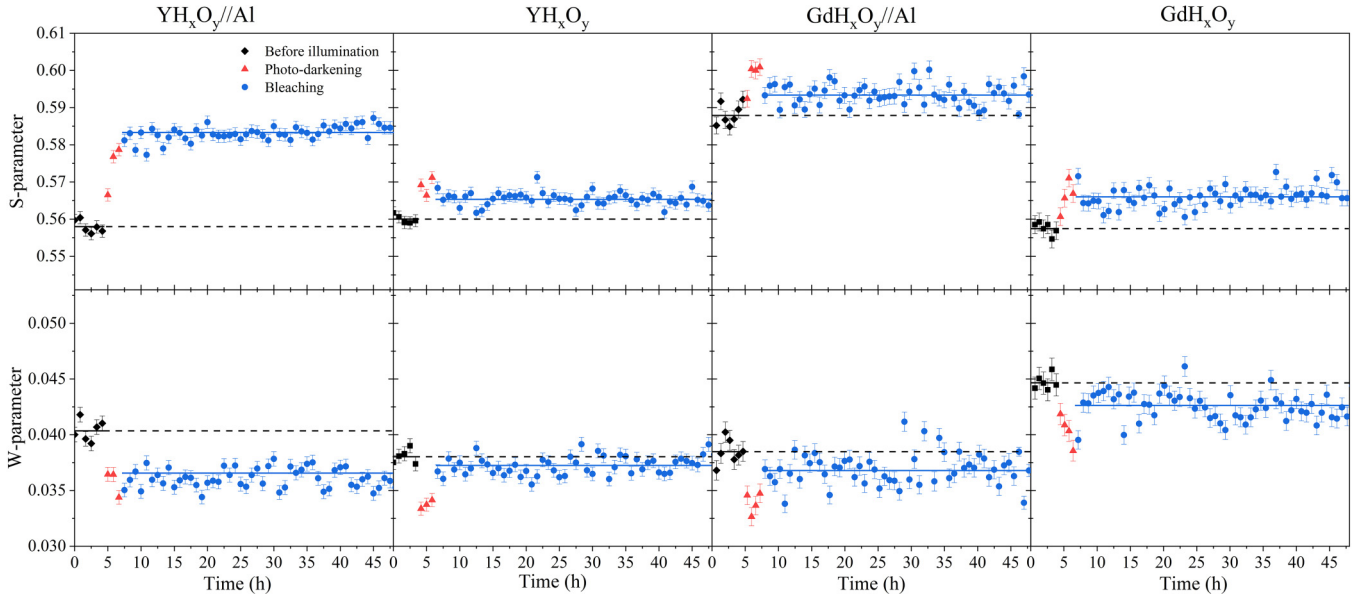

FIG. 5. Time dependence of the S and W Doppler broadening (DB) parameters collected in *in-situ* DB positron annihilation spectroscopy (DB-PAS) measurements on YH_xO_y//Al, uncapped YH_xO_y, GdH_xO_y//Al, and uncapped GdH_xO_y films before ultraviolet (UV) illumination (black symbols), under 2.5 h illumination (photodarkening, red triangles) and during ∼38 h of bleaching (blue circles) collected at positron implantation energies of 6.4, 5, 6.4, and 7.2 keV, respectively.

anions may play a role in the mechanism of the photochromic effect for both RE oxyhydride systems, as suggested previously in Refs. [8,50].

More insights into the evolution of the nanostructure of the oxyhydride layers were gained from the time dependence of the S and W parameters of the YH_xO_y//Al, uncapped YH_xO_y, GdH_xO_y//Al, and uncapped GdH_xO_y films before illumination, during UV photodarkening and during subsequent bleaching, collected at fixed positron implantation energies of 6.4, 5, 6.4, and 7.2 keV, respectively, as shown in Fig. 5. These positron implantation energies were selected to ensure that most of the positrons annihilate in the oxyhydride layer. For all samples, the S parameter shows a substantial increase during illumination, while the W parameter decreases strongly. In the case of the Al-capped YH_xO_y film, the S and W parameters do not change further during bleaching, demonstrating that irreversible changes take place that persist on a time scale of at least 38 h, i.e., long after optical transparency of the film has returned, in line with the corresponding depth profiles and as reported in Ref. [8]. In contrast, the S and W parameters of the other three samples show a partially reversed behavior once the illumination is stopped, as the S and W values are seen to move back into the direction of their initial values, suggesting that the nanostructural properties of the films partially return toward the initial state. Nevertheless, permanent changes are also seen for these samples, with shifted S and W parameters that remain stable during bleaching for ∼38 h, consistent with the depth profiles in Fig. 4. As discussed, these permanent changes are related to the formation of stable divacancies (or small vacancy clusters) during illumination. It is remarkable that the DB parameters, particularly the W parameter, show large changes during illumination which partially shift back to the original state upon bleaching in the uncapped YH_xO_y, Al-capped GdH_xO_y//Al, and uncapped GdH_xO_y films. This strongly suggests that a second type of nanostructural change occurs during illumination, which recovers during bleaching.

To gain more insights into the origin of the changes in S and W during illumination, we compare the evolution of the S and W parameters in an S-W diagram with those of the as-deposited metal, metal hydride, and metal oxide films, Y, $YH_{\sim 1.9}$, Y_2O_3, Gd, $GdH_{\sim 2}$, and Gd_2O_3, respectively. In Fig. 6, the S-W points are presented for YH_xO_y//Al, uncapped YH_xO_y, GdH_xO_y//Al, and uncapped GdH_xO_y films (1) before illumination, (2) upon 1.5 to 2.5 h of illumination, and (3) after illumination in the bleached state extracted from the time-dependence measurements at fixed positron implantation energy (Fig. 5), together with those of the as-deposited metal, metal hydride, and oxide films. The values of the S and W parameters are also given in Table SIV in the Supplemental Material [18]. The shifts in the (S,W) points of the YH_xO_y, GdH_xO_y//Al, and GdH_xO_y films during illumination (process 1 → 2) clearly are parallel to the line connecting the (S,W) points of the metal oxide RE_2O_3 and metal hydride REH_2 phases. The corresponding quantitative values of the parameter $R = \frac{\Delta S}{\Delta W}$, with ΔS and ΔW the change in respectively the S and W parameters induced by the illumination, for the oxyhydride films of $R = -2.0 \pm 0.5$ (YH_xO_y), -2.5 ± 0.5 (GdH_xO_y//Al), and -2.2 ± 0.7 (GdH_xO_y) are close to $R = -2.5 \pm 0.1$ for the line that connects the Y or Gd metal oxide and metal hydride. After the illumination is stopped and bleaching sets in, the shifts in the S-W diagram are partially reversed (process 2 → 3), suggesting that part of the illumination-induced nanostructural transformations is reversible, possibly related to formation and disappearance of metallic domains. In contrast, the illumination-induced shift in S-W for the Al-capped YH_xO_y film, with $R = -4 \pm 1$, is not exactly parallel to the line connecting the S-W points of Y_2O_3 and $YH_{\sim 1.9}$. Furthermore, in the bleaching phase, no sign of reversibility is observed for this sample, in line with

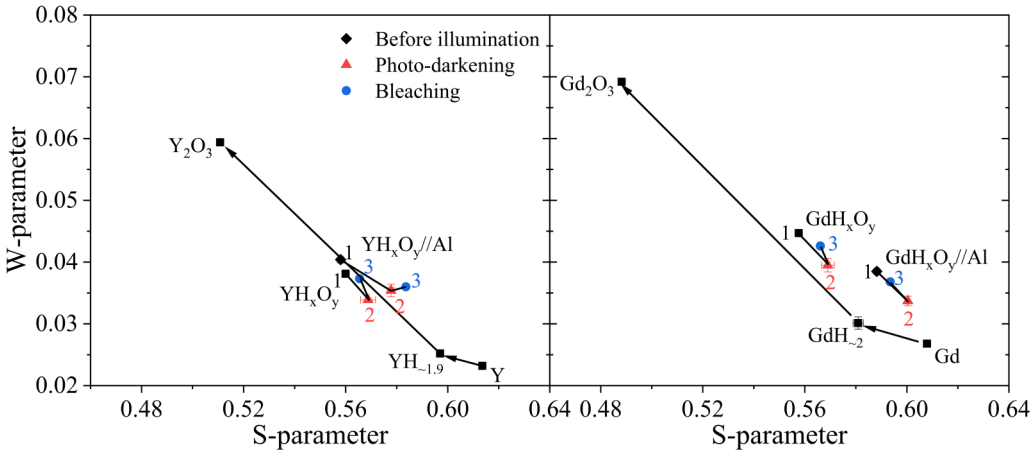

FIG. 6. S and W values for YH_xO_y//Al, uncapped YH_xO_y, GdH_xO_y//Al, and uncapped GdH_xO_y films before illumination (1, black symbols), upon illumination for 1.5–2.5 h (2, red triangles), and after illumination in the bleaching state (3, blue circles) according to the *in-situ* illumination Doppler broadening positron annihilation spectroscopy (DB-PAS) measurements compared with the (S,W) points of the as-deposited Y, Gd metal, $YH_{\sim1.9}$, $GdH_{\sim2}$ metal hydride, and YH_2O_3, Gd_2O_3 metal oxide films.

Ref. [8]. This could be due to a larger concentration of divacancies induced in this sample by the illumination, leading to a relatively large increase in S compared with the other samples. During bleaching, the metallic domains disappear, causing even more positrons to trap in divacancies during bleaching than the photodarkening state. In this case, the irreversible formation of divacancies (or small vacancy clusters) that act as positron trapping centers appears to be the dominant process. The increase in the S parameter indicates that the S parameter for divacancies is higher than for the metallic domains.

We note that the irreversible formation of divacancies occurs for all samples, as the R values obtained from a comparison of the as-prepared state with the state of the films after bleaching ($1 \rightarrow 3$) of $R = -7 \pm 1$ (YH_xO_y//Al), $R = -6.9 \pm 2.5$ (YH_xO_y), $R = -3.1 \pm 0.9$ (GdH_xO_y//Al), and $R = -4.0 \pm 0.8$ (GdH_xO_y) are larger than for the shifts in (S,W) observed during photodarkening. In view of the photochromism, the partially reversible behavior observed during bleaching for the latter three samples is significant and points to a second, reversible nanostructural process induced by the illumination in addition to the formation of vacancies and irreversible formation of divacancies. Below, we will discuss two proposed mechanisms that may contribute to the photodarkening and, at the same time, could explain the observed reversible part of the changes in the positron DB S and W parameters. These two proposed mechanisms are schematically illustrated in Fig. 7.

3. *Proposed mechanism 1: The formation of hydrogen-rich metallic-like nanodomains*

The observed shift of the S-W points for the oxyhydride films during UV illumination into the direction of the S-W point of the metal hydride suggests that the illumination leads to the formation of domains with lower O : H ratios (lower ionicity). Indeed, in our previous study [8], we found that YH_xO_y films synthesized at lower deposition pressure contain more hydrogen (lower O : H ratio) and exhibit systematically higher S and lower W parameters [8]. If we assume that the difference in the (S,W) point for YH_xO_y with respect to the (S,W) point of the metal oxide Y_2O_3 phase is proportional to its hydrogen fraction and that YH_xO_y deposited at 0.4 Pa (near the boundary pressure beyond which the films gain full optical transparency) corresponds to a composition close to $YH_2O_{0.5}$, the composition of the film deposited at 0.5 Pa would approximately correspond to $YH_{\sim1.7}O_{\sim0.65}$. Upon illumination, the (S,W) point of the 0.5 Pa sample approaches that of the as-prepared 0.4 Pa sample, suggesting that the domains probed by the positrons contain a hydrogen-enriched composition that is, on the average, close to that of $YH_2O_{0.5}$. The picture, thus, emerges that, during UV illumination, some hydrogen ions are released from their lattice positions, possibly from the energetically less favorable octahedral sites [51,52], due

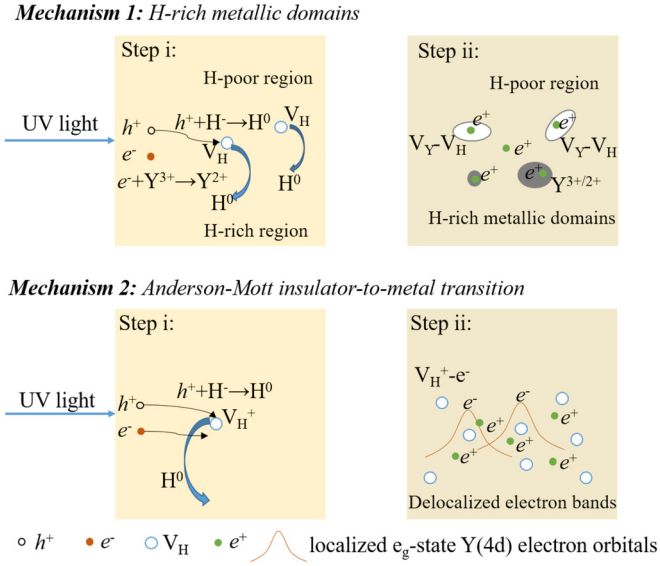

FIG. 7. Schematic illustration of the proposed mechanisms 1 and 2.

to the light-induced formation of mobile neutral hydrogen by the excitation of electron-hole pairs with $H^- + h^+ \rightarrow H^0$. Subsequently, the mobile neutral hydrogen ions move toward a local environment with lower oxygen content and form hydrogen-enriched domains. If the local composition reaches an O : H ratio below that of $YH_2O_{0.5}$, particularly YH_2O_x with $x < 0.5$, a mixed valence character of the Y cations sets in, with part of the Y^{3+} replaced by Y^{2+}, and the electronic structure becomes metallic-like for a sufficiently high local concentration of Y^{2+}. Alternatively, the mentioned removal of hydrogen atoms in combination with a local displacement of an oxygen ion to the site of 1 out of 2 removed hydrogen atoms can lead to local phase segregation into a hydrogen-poor area and a metallic hydrogen-rich area with a local composition of YH_2O_x ($x < 0.5$), for example, according to $2Y_4H_8O_2 \rightarrow Y_4H_8O_2 + Y_4H_6O_2 + 2H^0 \rightarrow Y_4H_8O + Y_4H_6O_3 + 2H^0$, with the resulting $YH_2O_{0.25}$ in a mixed Y^{2+}/Y^{3+} valence state, while the hydrogen-poor $YH_{1.5}O_{0.75}$ fully retains the Y^{3+} valence state. Both mentioned options suggest that phase-segregated domains with a metallic-like character are formed during illumination, enabled by mobility of light-induced interstitial hydrogen (supported also by the observation of release of a small amount of hydrogen molecules from YH_xO_y films during UV illumination [53]) and local displacements of oxygen ions. Indeed, molecular dynamics simulations suggest hopping mobility primarily of hydrogen located at octahedral sites, but a small hopping mobility of oxygen is also seen [52]. The occurrence of the phase segregation process is supported by previous spectroscopic ellipsometry studies that suggested that metallic domains at a volume fraction of up to ∼6 vol. % are formed during the illumination [14], leading to pronounced changes in the dielectric function in the near-IR and visible range. NMR studies on YH_xO_y films suggest relocation of the hydrogen in the lattice during the illumination, reporting the disappearance of a ∼3% mobile hydrogen fraction seen in ^1H magic angle spinning, which recovers after bleaching in the dark [15]. The formation of such metallic-like domains in an otherwise semiconducting (transparent) matrix may explain the reduction in optical transmission over a large subbandgap wavelength range [14], characteristic for the photochromic effect in this class of RE oxyhydrides. Remarkably, such changes in the optical properties also occur by modification of the composition to $Y_{1-z}Zr_zH_xO_y$ by cosputtering of Y and Zr [54]. For these mixed cation oxyhydride films, the addition of Zr leads to a strong reduction in the optical transmission in the subbandgap wavelength range ($T \sim 86\%$ for $z = 0$ to $T \sim 62\%$ for $z = 0.5$), while the reflectivity R stays relatively small ($R \sim 12\%$ for $z = 0$ to $R \sim 15\%$ for $z = 0.5$; with $R \sim 12\%$ for YO_xH_y films mainly related to the index of refraction in the range of $n \sim 1.9$–2.2 [14,55]), and the subbandgap optical absorption is increased, attributed to the presence of not fully oxidized metallic ZrH_2 clusters in the otherwise semiconducting $Y_{1-z}Zr_zH_xO_y$ films (with bandgaps in the range of 2.2–2.8 eV) [54].

We note that the observed remarkably large change in the positron DB W parameter (∼12%) and the corresponding clear shift in the S parameter in these films upon illumination can be attributed within this proposed mechanism to either a high concentration of H-rich domains or a high fraction of positrons annihilating in H-rich domains. Since the formation of H-rich domains is necessarily accompanied by the formation of H-poor domains (as we assume no H enters or diffuses out of the film), one could expect that the values for S and W averaged over the volume of the oxyhydride film do not change much. Therefore, the large reversible part of the changes in S and W observed during illumination requires a high fraction of positrons after diffusion in the film traps and annihilates in the H-rich domains. Such preferential trapping of positrons can be caused by a larger positron affinity for H-rich regions than H-poor regions and can have a pronounced effect on the positron signal even when only a relatively small amount of nanosized H-rich domains is present. For instance, in previous positron DB and two-dimensional ACAR studies of metallic Li nanoclusters embedded in crystalline MgO [56], a positron trapping fraction in the Li nanoclusters as high as ∼92% was observed with only ∼3 vol. % of Li nanoclusters present in the MgO matrix [56]. In that study, the preferred positron trapping in the Li nanodomains was caused by the large difference in the positron affinity for Li compared with MgO (∼1.8–2.8 eV) deduced from *ab initio* calculations [46,56]. We should note that, in the present case, during illumination, not only H-rich domains are formed but also cation-anion divacancies such as V_Y-V_H in the H-poor oxyhydride matrix. Thus, during illumination, preferential trapping of positrons not only occurs at H-rich metallic domains but also at V_Y-V_H in the H-poor regions (Fig. 7). Both processes contribute to the observed changes in S and W during illumination. For simplicity, we did not include the process of divacancy formation in the oxyhydride matrix, which might reduce the positron diffusion length, in our simulations.

A similar amplifying effect of the positron signal from embedded metallic nanodomains could also take place for the photodarkened oxyhydrides, provided that (1) the average distance between H-enriched domains that appear during illumination are of the same order of magnitude or less than the diffusion length of positrons in the surrounding H-poor oxyhydride matrix, and (2) the difference in positron affinity is sufficiently large, i.e., at least several tenths of an electronvolt to prevent significant thermal detrapping.

To assess the implications of preferred positron trapping quantitatively, we present simulations on the fraction of positrons that annihilate in such H-enriched domains following the diffusion-limited trapping model used in Refs. [56,57]. This model assumes that the domains are spherical in shape and homogeneously distributed in the matrix. We assume that all positrons that reach H-rich domains are trapped and that detrapping of positrons from the domains can be neglected. The fraction of positrons that are initially stopped in the matrix and subsequently trap in H-rich domains f_{domains} is then given by Eqs. (4) and (5) [56,57]:

$$f_{\text{domains}} = \frac{\kappa}{\kappa + \lambda_{\text{matrix}}} = \frac{4\pi r D_+ c}{4\pi r D_+ c + \lambda_{\text{matrix}}} = \frac{4\pi r L_+^2 c}{4\pi r L_+^2 c + 1}, \tag{4}$$

$$L_+ = \sqrt{D_+/\lambda_{\text{matrix}}}, \tag{5}$$

where κ is the positron trapping rate in the hydrogen-rich metallic-like domains (s^{-1}), λ_{matrix} is the effective annihilation rate in the oxyhydride matrix surrounding the domains (s^{-1}), r is the radius of the domains (m), c is the concentration of the domains (m^{-3}), D_+ and L_+ are, respectively, the positron diffusion coefficient ($m^2\,s^{-1}$) and positron diffusion length in the oxyhydride matrix (m). Equation (4) can be rewritten in terms of the volume fraction of metallic domains f_V, the radius of a metallic domain r, and the positron diffusion length L_+, according to $f_{domains}(r) = \frac{f_V 3L_+^2}{f_V 3L_+^2 + r^2}$.

While the size of the H-rich domains formed in the oxyhydride films is not known, their size must be larger than ~0.5 nm since the positrons cannot trap if the domain size is too small, as the difference in positron affinity with the surrounding matrix will disappear due to the increase in the energy of the quantum confined positron state with reduced domain size [56]. On the other hand, if the size of the H-rich domains is large at a low (constant) volume fraction of H-rich domains, the concentration of domains will be small. The probability of positron trapping in the domains will be low in that case due to the large average distance between the H-rich domains. This distance then becomes much larger than the positron diffusion length in the H-poor oxyhydride matrix, and only a small fraction of positrons will be able to reach the H-rich domains and annihilate there instead of the surrounding matrix.

As an example of our simulations, we first consider the case of H-rich domains with a radius of 1 nm occupying a volume fraction of 6 vol. % of the oxyhydride. The concentration of the domains will then be $\sim 1.4 \times 10^{25}\,m^{-3}$, corresponding to an average interdomain distance of ~4 nm. We assume that the diffusion length L_+ in oxyhydride films is 20 nm since the experimental diffusion length extracted from the VEPFIT analysis of the oxyhydride films ranges from ~10 to ~40 nm (Table SV in Supplemental Material [18]), i.e., reduced with respect to the estimated diffusion length of ~150 nm for defect-free yttrium oxyhydride by positron trapping in vacancies with a concentration of $\sim 10^{-4}$ [48] (see Supplemental Material [18]). These parameters yield a very high fraction of ~99% of positrons that trap and annihilate in domains with a radius of 1 nm. This illustrates that, despite a low volume fraction, the positron signal can be dominated by annihilation in H-rich domains. We note that, in this model, the fraction of positrons trapping in the H-rich domains is significantly affected by the average distance between the domains (that scales proportional to the size of the domains for a given volume fraction) and by the positron diffusion length in the H-poor matrix. If we consider that a fraction of the implanted positrons will be stopped inside of the metallic domains instead of the matrix, the full expression for the fraction of positrons annihilating in the metallic domains is $f_{domains}(r) = (1 - f_V)\frac{f_V 3L_+^2}{f_V 3L_+^2 + r^2} + f_V$, assuming that the mass density of the domains and the matrix are comparable.

In Fig. 8, we therefore show the simulated dependence of the fraction of positrons that annihilate in the H-rich domains $f_{domains}$ on the average distance between (and size of) these domains, for three different positron diffusion lengths of 10, 20, and 40 nm, respectively, for a volume fraction $f_V = 0.06$ (6 vol. %) of H-rich domains with radius r.

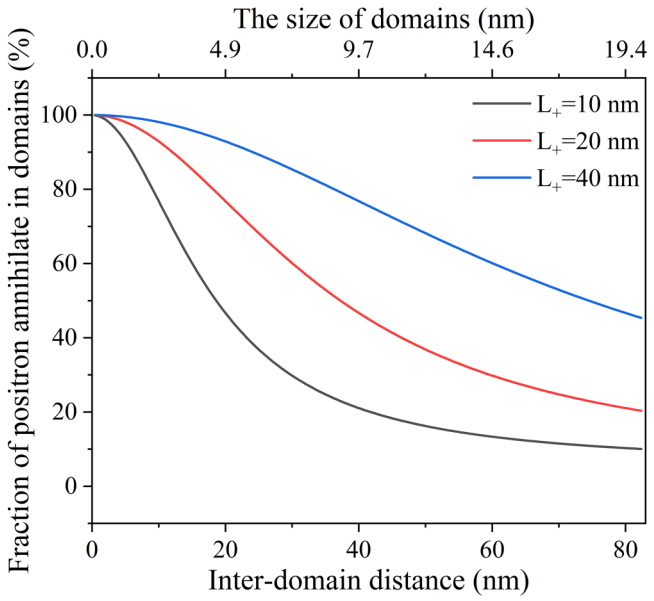

FIG. 8. Simulated positron annihilation fractions in H-rich domains as a function of average distance between the domains at positron diffusion lengths of 10, 20, and 40 nm, respectively. A volume fraction of 6 vol. % of spherically shaped domains was assumed.

The positron annihilation fractions in the H-rich domains are much higher in most areas of Fig. 8 than what would be expected solely based on a volume fraction of ~6 vol. % of these domains. This shows that H-rich domains at a small volume fraction can dominate the positron signal in certain parameter regions. Our simulations suggest that the average size of the H-rich domains (at a volume fraction of 6 vol. %) should be in the range of ~0.5 to ~20 nm in case the observed shifts in (S,W) parameters (Fig. 6) are caused by the formation of H-rich domains in a H-reduced YO_xH_y matrix.

4. Proposed mechanism 2: Anderson-Mott insulator-to-metal transition in domains related to electron states localized near formed hydrogen vacancies

A second possible mechanism that we discuss here is inspired by the insulator-to-metal transition in yttrium trihydride and lanthanum trihydride, which exhibit large changes in the optical properties and conductivity upon release of hydrogen when a composition of respectively $YH_{\sim 2.7}$ and $LaH_{\sim 2.8}$ is reached. According to Ng *et al.* [58], the insulator-to-metal transition is induced by the formation of hydrogen vacancies at octahedral sites (V_H^+), where charge-compensating electrons are localized in an e_g-state Y($4d$) electron orbital at the surrounding Y ions. When the concentration of these localized electrons is sufficient high, their orbitals overlap, leading to the formation of a delocalized electron band and the occurrence of the insulator-to-metal transition.

We assume that a similar scenario may play a role in the photochromism of the RE oxyhydride films. When such oxyhydride films are exposed to UV light with photon energy above the bandgap, electron-hole (e^--h^+) pairs are generated. The positively charged holes may be trapped by H^- anions

and form neutral hydrogen (H^0) according to $H^- + h^+ \rightarrow H^0$. The neutral hydrogen will subsequently be released from its lattice position. Since hydrogen atoms are less strongly bound at the octahedral sites [51,52], this process will occur predominantly for octahedral site hydrogen, and hydrogen vacancies are formed at octahedral sites, like the case of YH_3 and LaH_3, carrying a positive charge V_H^+.

The released H^0 might stay at interstitial positions or get trapped at the vacancy clusters or nanopores inside the films, or like what occurs in YH_3 and LaH_3, even effuse out of the films. Simultaneously, the photoexcited electrons present in the conduction band of the REH_xO_y will sense the Coulomb force of the positively charged V_H^+ centers and may get trapped in a localized e_g-Y($4d$) orbital of the Y ions surrounding a hydrogen vacancy, as this will constitute a strongly bonded state with binding energies of the order of several electronvolts [58]. Progressive illumination will lead to continuous creation of e^--h^+ pairs. Consequently, the concentration of V_H^+ vacancies will gradually increase in time. When the concentration of octahedral V_H^+ in a certain domain of the YH_xO_y film is sufficient large, say, of the order of ∼10% of the hydrogen present in the domains (as required for yttrium trihydride, YH_3), one can expect the orbitals of the trapped charge-compensating localized e_g-state Y($4d$) electrons to overlap. This will lead to the formation of an electron band and a metallic-like electronic structure of the respective domains in the YH_xO_y film, inducing the Anderson-Mott insulator-to-metal transition in these domains in the RE oxyhydride films under illumination. We note in addition, that such a high concentration of delocalized electrons is observable in positron DB, which would lead to a shift in (S,W) to higher S and lower W parameters approximately toward the direction of the (S,W) point of the metallic dihydride.

It is interesting to discuss the implications of this proposed mechanism for the time scale of the photodarkening process in a semiquantitative manner. If we assume that, to induce photodarkening, a significant fraction of neutral charge H atoms need to be removed from octahedral sites of, for example, $YH_2O_{0.5}$, according to $Y_4H_8O_{0.5} \rightarrow Y_4H_7O_{0.5} + H^0$ (∼12.5% of the hydrogen removed), ∼1 hydrogen vacancy will be formed on the average in a cubic unit cell with lattice parameter of ∼0.54 nm. Following this, a required hydrogen vacancy density of $\sim 6.4 \times 10^{21}\,cm^{-3}$ can be estimated. On the other hand, the photon flux of the LED used in the present *in-situ* illumination DB-PAS studies is $\sim 6.6 \times 10^{16}$ photons $cm^{-2}\,s^{-1}$. Assuming that all incident photons are absorbed in the ∼300-nm-thick YH_xO_y film, one can estimate an average density of absorbed photons per second of $\sim 2.2 \times 10^{21}$ photons $cm^{-3}\,s^{-1}$. If each photon is converted into an electron-hole pair and leads to the generation of a hydrogen vacancy-localized electron pair at 100% conversion efficiency, one can estimate that a time on the order of a few seconds would be required to induce the insulator-to-metal transition. This estimated time scale needed for photodarkening of the films is clearly much longer than typical for photoexcited carrier processes in opto-electric materials such as solar cells (on the order of nanoseconds to microseconds) [59]. The initial stages of the photodarkening in the RE oxyhydride films indeed take place at a seconds timescale but slow down in the process toward saturation. For instance, $\sim\frac{1}{3}$ of the total change in transmittance upon UV illumination of both YH_xO_y and GdH_xO_y films (Fig. 3) occurs within the first 30 s. Clearly, therefore, the observed time scales for photodarkening in these RE oxyhydride films, which in the initial phase are an order of magnitude larger than the theoretical estimate, can be understood well within this proposed mechanism since most of the abovementioned processes will likely not be highly efficient.

The abovementioned parameters can also be used to give a qualitative insight into the optical properties associated with the photodarkening phenomenon in oxyhydride films, in which a substantial reduction in the transmittance in a broad subbandgap wavelength range (above ∼400 nm) is observed after illumination, related to a strong increase in absorption. In simple free-electron metals, strong increase in reflectance is primarily caused by prohibition of propagation of light waves within the metal at frequencies around and below plasma frequency ω_p since the index of refraction becomes predominantly imaginary, and collision losses of conduction electrons may lead to strong absorption [60,61]. The plasma frequency ω_p is given by $\omega_p = \sqrt{\frac{ne^2}{\epsilon_0 m^*}}$, where n is density of electrons, e the electron charge, ϵ_0 the dielectric permittivity of the vacuum, and m^* is the effective electron mass, respectively. Accordingly, the plasma wavelength λ_p is given by $\lambda_p = \frac{2\pi c}{\omega_p}$, where c is the velocity of light in the vacuum. We assume, in this simple free-electron (Drude-like) picture, that the effective electron mass is equal to its rest mass. Based on the assumption that a delocalized electron band is formed in domains of the YH_xO_y film when the local electron density reaches $\sim 6.4 \times 10^{21}\,cm^{-3}$ (i.e., for the case of 12.5% hydrogen vacancies in $YH_2O_{0.5}$), a plasma frequency ω_p and a plasma wavelength λ_p of $\sim 4.5 \times 10^{15}\,s^{-1}$ and ∼420 nm, respectively, can be estimated. For a macroscopic, free-electron metal, this plasma resonance results in a high reflectivity $R \sim 1$ for wavelengths longer than the plasma wavelength. However, in the case of a metallic domain of size smaller or comparable with the incident wavelength, the confinement in space of the free-electron gas leads to a more complex situation better described by the Mie theory [62,63]. Here, as the oscillating electromagnetic field drives the electron gas against the surfaces of the metallic domain, an oscillating dipole/multipole is induced, and a fraction of the incoming radiation energy is absorbed in the polarization of the metal/dielectric interface. A further fraction of the incoming energy is scattered as radiation from the oscillating dipole/multipole. The presence of domains with a metallic-like character in the illuminated RE oxyhydride films may explain their largely changed optical properties in the photodarkened state, e.g., the large reduction in optical transmission in a wide subbandgap wavelength range (above ∼400 nm). Future studies are required to simulate the optical properties of metallic domains embedded in a semiconducting YH_xO_y medium, which may include plasmonic resonances that depend on the size and shape of the domains as well as on their electron concentration. Also, *ab initio* calculations of the electronic structure of the formed electron band are a promising future research direction to

gain advanced insights into the mechanism proposed in this section.

Finally, we note that this proposed mechanism is also in line with the observed gradual reduction in the photochromic contrast with increased O : H ratio, for compositions of $x\sim0.5$–1 for magnetron-sputtered $YH_{3-2x}O_x$ films [8]. In this composition range, a systematic decrease occurs in the number of hydrogen atoms located at octahedral sites. This leads to a reduction in the (maximum) concentration of octahedral vacancies that can be generated by the illumination. Consequently, this reduces the probability that, in a certain nanoscale area, the threshold concentration of electrons is reached required for the formation of the (free-)electron band that, within this proposed mechanism, underlies the (local) insulator-to-metal transition and corresponding changes in the optical properties of the film under illumination.

IV. CONCLUSIONS

The sizes and concentrations of open volume defects in as-prepared magnetron sputtered YH_xO_y, Y, $YH_{\sim1.9}$, and Y_2O_3 thin films were studied by PALS. It was found that yttrium cation monovacancies dominate the positron annihilation signal in Y and Y dihydride thin films at concentrations on the order of 10^{-5} per Y atom. The concentration of monovacancies extracted by DB-PAS is on the order of 10^{-4}. Thus, we conclude that the concentration of monovacancies is in the range of 10^{-5} to 10^{-4}. Furthermore, larger vacancy clusters are also present at lower concentrations. In addition, the formation of positronium (Ps) in the YH_xO_y and Y_2O_3 thin films is observed, revealing the presence of nanopores. The systematic changes of electronic structure of RE metal, metal dihydride, semiconducting metal oxyhydride, and insulating metal oxide films upon varying the O and H contents of the films were seen in the S-W diagrams extracted from positron DB experiments. The nanostructural evolution in photochromic Al-capped and uncapped Y/Gd oxyhydride films upon illumination is studied by *in-situ* DB-PAS. For the YO_xH_y//Al film, a pronounced increase in the S parameter and decrease in the W parameter result from the 2.5 h illumination and remain stable during ∼38 h bleaching. This indicates that UV illumination induces the formation of anion vacancies by releasing anions from their lattice positions. Part of the anion vacancies cluster subsequently with V_Y monovacancies in an irreversible manner, resulting in the formation of stable divacancies. For the YO_xH_y, GdO_xH_y//Al, and GdO_xH_y films, partially reversible shifts of their S-W points in the direction of the S-W point of the RE metal hydride were observed during photodarkening, indicating the formation of metallic domains. Two proposed mechanisms for the formation of metallic domains in these RE oxyhydride films during illumination are discussed. The first proposed mechanism suggests the formation of phase-segregated H-rich domains, enabled by hydrogen liberated from their lattice positions during illumination and possibly local oxygen displacement. The strong shifts in the S and W parameters can be explained by preferred trapping of positrons in the phase-segregated nanosized H-rich metallic-like domains, as supported by our simulations using a diffusion-limited trapping model. This supports proposed mechanisms for the photochromic effect in these RE oxyhydrides based on the formation of metallic-like nanosized domains. The second proposed mechanism is based on the formation of positively charged hydrogen vacancies at octahedral sites enabled by hydrogen liberated during illumination, with charge-compensating Y($4d$) e_g-state electrons localized at the surrounding Y ions. When the concentration of these e_g-state electrons in certain domains in the REH_xO_y film is sufficiently high, their orbitals overlap and a (free-)electron band is formed, causing metallicity of these domains, resulting in photodarkening of the film. This mechanism can qualitatively explain the timescale of photodarkening, the reduction in optical transmission over a large subbandgap wavelength interval, and the systematic reduction in photochromic contrast for compositions with increased O : H ratios.

ACKNOWLEDGMENTS

This paper was financially supported by Guangzhou Elite Project and the Materials for Sustainability programme (Grant No. 680.M4SF.034) of the Dutch Research Council. The authors thank the MLZ, Garching, Germany, for providing the positron beamtime at the PLEPS instrument of the NEPOMUC facility, and Herman Schreuders for technical support.

[1] Y. J. Ke, J. W. Chen, C. J. Lin, S. C. Wang, Y. Zhou, J. Yin, P. S. Lee, and Y. Long, Smart windows: electro-, thermo-, mechano-, photochromics, and beyond, Adv. Energy Mater. **9**, 1902066 (2019).

[2] A. D. Towns, in *Applied Photochemistry: When Light Meets Molecules*, edited by G. Bergamini and S. Silvi (Springer International Publishing, Cham, 2016), pp. 227.

[3] K. Yoshimura, C. Langhammer, and B. Dam, Metal hydrides for smart window and sensor applications, MRS Bull. **38**, 495 (2013).

[4] S. F. Wang, W. R. Fan, Z. C. Liu, A. B. Yu, and X. C. Jiang, Advances on tungsten oxide based photochromic materials: strategies to improve their photochromic properties, J. Mater. Chem. C **6**, 191 (2018).

[5] G. P. Smith, Photochromic glasses: properties and applications, J. Mater. Sci. **2**, 139 (1967).

[6] T. Mongstad, C. Platzer-Bjorkman, J. P. Maehlen, L. P. A. Mooij, Y. Pivak, B. Dam, E. S. Marstein, B. C. Hauback, and S. Z. Karazhanov, A new thin film photochromic material: oxygen-containing yttrium hydride, Sol. Energy Mat. Sol. Cells **95**, 3596 (2011).

[7] F. Nafezarefi, H. Schreuders, B. Dam, and S. Cornelius, Photochromism of rare-earth metal-oxy-hydrides, Appl. Phys. Lett. **111**, 103903 (2017).

[8] G. Colombi, T. de Krom, D. Chaykina, S. Cornelius, S. W. H. Eijt, and B. Dam, Influence of cation (RE = Sc, Y, Gd) and O/H anion ratio on the photochromic properties of REO_xH_{3-2x} thin films, ACS Photonics **8**, 709 (2021).

[9] S. Cornelius, G. Colombi, F. Nafezarefi, H. Schreuders, R. Heller, F. Munnik, and B. Dam, Oxyhydride nature of rare-earth-based photochromic thin films, J. Phys. Chem. Lett. **10**, 1342 (2019).

[10] C. C. You, T. Mongstad, E. S. Marstein, and S. Z. Karazhanov, The dependence of structural, electrical and optical properties on the composition of photochromic yttrium oxyhydride thin films, Materialia **6**, 100307 (2019).

[11] C. C. You, T. Mongstad, J. P. Maehlen, and S. Karazhanov, Engineering of the band gap and optical properties of thin films of yttrium hydride, Appl. Phys. Lett. **105**, 031910 (2014).

[12] D. Moldarev, M. V. Moro, C. C. You, E. M. Baba, S. Z. Karazhanov, M. Wolff, and D. Primetzhofer, Yttrium oxyhydrides for photochromic applications: correlating composition and optical response, Phys. Rev. Materials **2**, 115203 (2018).

[13] H. J. Hoffmann, *Photochromic Glasses, The Properties of Optical Glass* (Springer, Berlin, Heidelberg, 1998).

[14] J. Montero, F. A. Martinsen, M. Garcia-Tecedor, S. Z. Karazhanov, D. Maestre, B. Hauback, and E. S. Marstein, Photochromic mechanism in oxygen-containing yttrium hydride thin films: an optical perspective, Phys. Rev. B **95**, 201301(R) (2017).

[15] C. V. Chandran, H. Schreuders, B. Dam, J. W. G. Janssen, J. Bart, A. P. M. Kentgens, and P. J. M. van Bentum, Solid-state NMR studies of the photochromic effects of thin films of oxygen-containing yttrium hydride, J. Phys. Chem. C **118**, 22935 (2014).

[16] M. P. Plokker, S. W. H. Eijt, F. Naziris, H. Schut, F. Nafezarefi, H. Schreuders, S. Cornelius, and B. Dam, Electronic structure and vacancy formation in photochromic yttrium oxy-hydride thin films studied by positron annihilation, Sol. Energy Mat. Sol. Cells **177**, 97 (2018).

[17] J. N. Huiberts, R. Griessen, J. H. Rector, R. J. Wijngaarden, J. P. Dekker, D. G. de Groot, and N. J. Koeman, Yttrium and lanthanum hydride films with switchable optical properties, Nature (London) **380**, 231 (1996).

[18] See Supplemental Material at http://link.aps.org/supplemental/10.1103/PhysRevMaterials.6.065201 for the list of additional samples, XRD, positron annihilation fractions for each layer as a function of implantation energy, PALS, positron lifetime parameters, optical transmittance spectra, Tauc plot analysis of the optical bandgap, and the S and W values from DB positron annihilation experiments.

[19] H. M. Rietveld, A profile refinement method for nuclear and magnetic structures, J. Appl. Crystallogr. **2**, 65 (1969).

[20] J. Rodriguez-Carvajal, FULLPROF: a program for Rietveld refinement and pattern matching analysis, Satellite Meeting on Powder Diffraction of the XV Congress of the IUCr, Toulouse (1990).

[21] M. Zhang, M. A. Farid, H. Zhang, J. L. Sun, G. B. Li, F. H. Liao, and J. H. Lin, Superconductivity of perovskite $Ba_{1-x}Y_x(Bi_{0.2}Pb_{0.8})O_{3-\delta}$, J. Supercond. Nov. Magn. **30**, 1705 (2017).

[22] P. Sperr, W. Egger, G. Kögel, G. Dollinger, C. Hugenschmidt, R. Repper, and C. Piochacz, Status of the pulsed low energy positron beam system (PLEPS) at the Munich Research Reactor FRM-II, Appl. Surf. Sci. **255**, 35 (2008).

[23] C. Hugenschmidt, B. Löwe, J. Mayer, C. Piochacz, P. Pikart, R. Repper, M. Stadlbauer, and K. Schreckenbach, Unprecedented intensity of a low-energy positron beam, Nucl. Instrum. Meth. A **593**, 614 (2008).

[24] C. Hugenschmidt, C. Piochacz, M. Reiner, and K. Schreckenbach, The NEPOMUC upgrade and advanced positron beam experiments, New J. Phys. **14**, 055027 (2012).

[25] D. Bochert, Optimierte Analyse von Lebenszeitspektren aus Positronenstrahlsystemen, Diplom Arbeit, Universität der Bundeswehr München, München, 2004.

[26] W. Egger, P. Sperr, G. Kögel, M. Wetzel, and H. J. Gudladt, Investigations of epoxy-based adhesives with PLEPS, Appl. Surf. Sci. **255**, 209 (2008).

[27] H. Schut, A Variable Energy Positron Beam Facility with Applications in Materials Science, Ph.D. thesis, Delft University of Technology, Delft, 1990.

[28] A. van Veen, H. Schut, J. de Vries, R. A. Hakvoort, and M. R. IJpma, Analysis of positron profiling data by means of VEPFIT, AIP Conf. Proc. **218**, 171 (1990).

[29] R. Krause-Rehberg and H. S. Leipner, *Positron Annihilation in Semiconductors—Defect Studies* (Springer-Verlag, Berlin, 1999).

[30] M. J. Puska, C. Corbel, and R. M. Nieminen, Positron trapping in semiconductors, Phys. Rev. B **41**, 9980 (1990).

[31] J. M. C. Robles, E. Ogando, and F. Plazaola, Positron lifetime calculation for the elements of the periodic table, J. Phys. Condens. Mat. **19**, 176222 (2007).

[32] H. Leegwater, H. Schut, W. Egger, A. Baldi, B. Dam, and S. W. H. Eijt, Divacancies and the hydrogenation of Mg-Ti films with short range chemical order, Appl. Phys. Lett. **96**, 121902 (2010).

[33] A. Anastasopol, S. W. H. Eijt, H. Schut, F. M. Mulder, F. Plazaola, and B. Dam, Thermal stability of Mg_yTi_{1-y} thin films investigated by positron annihilation spectroscopy, Phys. Procedia **35**, 16 (2012).

[34] S. Assali, M. Elsayed, J. Nicolas, M. O. Liedke, A. Wagner, M. Butterling, R. Krause-Rehberg, and O. Moutanabbir, Vacancy complexes in nonequilibrium germanium-tin semiconductors, Appl. Phys. Lett. **114**, 251907 (2019).

[35] M. Elsayed, N. Y. Arutyunov, R. Krause-Rehberg, G. A. Oganesyan, and V. V. Kozlovski, Formation and annealing of vacancy-P complexes in proton-irradiated germanium, Acta Mater. **100**, 1 (2015).

[36] M. Eldrup, D. Lightbody, and J. N. Sherwood, The temperature-dependence of positron lifetimes in solid pivalic acid, Chem. Phys. **63**, 51 (1981).

[37] S. J. Tao, Positronium annihilation in molecular substances, J. Chem. Phys. **56**, 5499 (1972).

[38] L. C. Damonte, M. A. Taylor, J. Desimoni, and J. Runco, PALS study on the defect structure of yttria-stabilized zirconia, Radiat. Phys. Chem. **76**, 248 (2007).

[39] J. Brown, P. Mascher, and A. H. Kitai, Positron lifetime spectroscopy and cathodoluminescence of polycrystalline terbium-doped yttria, J. Electrochem. Soc. **142**, 958 (1995).

[40] J. Kuriplach and B. Barbiellini, Parameter-free gradient correction for positron states in oxides, Defect Diffus. Forum **373**, 35 (2017).

[41] B. Rozenfeld and E. Debowska, Investigation of the electronic structure of yttrium hydrides by positron annihilation, Acta Phys. Pol. A **47**, 37 (1975).

[42] I. Y. Dekhtyar and V. I. Shevchenko, Positron-annihilation in hydrides of transition-metals, Phys. Status Solidi B **83**, 323 (1977).

[43] W. J. Legerstee, J. de Roode, A. Anastasopol, C. V. Falub, and S. W. H. Eijt, In-situ hydrogen sorption 2D-ACAR facility for the study of metal hydrides for hydrogen storage, Phys. Proc. **35**, 22 (2012).

[44] A. Karjalainen, V. Prozheeva, K. Simula, I. Makkonen, V. Callewaert, J. B. Varley, and F. Tuomisto, Split Ga vacancies and the unusually strong anisotropy of positron annihilation spectra in β-Ga_2O_3, Phys. Rev. B **102**, 195207 (2020).

[45] J. Heikinheimo, S. Ortner, I. Makkonen, J. Kujala, M. Blackmur, and F. Tuomisto, Positron annihilation analysis of the atomic scale changes in oxidized Zircaloy-4 samples, J. Nucl. Mater. **495**, 172 (2017).

[46] C. V. Falub, P. E. Mijnarends, S. W. H. Eijt, M. A. van Huis, A. van Veen, and H. Schut, Electronic structure and orientation relationship of Li nanoclusters embedded in MgO studied by depth selective positron annihilation two-dimensional angular correlation, Phys. Rev. B **66**, 075426 (2002).

[47] J. Tauc, R. Grigorovici, and A. Vancu, Optical properties and electronic structure of amorphous germanium, Phys. Status Solidi B **15**, 627 (1966).

[48] We note that vacancy concentrations in the uncapped YH_xO_y film extracted from the diffusion length L_+ from DB-PAS depth profiling gives the monovacancy concentration in the range of $\sim 6 \times 10^{-5}$ to 1.5×10^{-4}, which is an order of magnitude larger than the values extracted by PALS. This could stem from either the closeness to saturation trapping in PALS or from the fact that the fitted positron diffusion length can be affected by, e.g., compositional or defect gradients. In view of the lower accuracy offered by using the diffusion length as a parameter to extract concentrations, we conclude that the concentration of monovacancies is in the range of 10^{-5} to 10^{-4} [49].The detailed calculation of vacancy concentrations extracted using positron diffusion lengths L_+ determined in the VEPFIT analysis can be found in the Supplemental Material [18].

[49] J. Cizek, F. Lukac, I. Prochazka, R. Kuzel, Y. Jiraskova, D. Janickovic, W. Anwand, and G. Brauer, Characterization of quenched-in vacancies in Fe-Al alloys, Physica B **407**, 2659 (2012).

[50] D. Chaykina, T. de Krom, G. Colombi, H. Schreuders, A. Suter, T. Prokscha, B. Dam, and S. Eijt, Structural properties and anion dynamics of yttrium dihydride and photochromic oxyhydride thin films examined by *in situ* μ^+ SR, Phys. Rev. B **103**, 224106 (2021).

[51] G. Colombi, S. Cornelius, A. Longo, and B. Dam, Structure model for anion-disordered photochromic gadolinium oxyhydride thin films, J. Phys. Chem. C **124**, 13541 (2020).

[52] R. Stigter, A Computational Investigation on the Structure of Yttrium Oxyhydride Compounds and Their Anion Mobility, MSc thesis, Delft University of Technology, Delft, 2020.

[53] D. Moldarev, L. Stolz, M. V. Moro, S. M. Adalsteinsson, I. A. Chioar, S. Z. Karazhanov, D. Primetzhofer, and M. Wolff, Environmental dependence of the photochromic effect of oxygen-containing rare-earth metal hydrides, J. Appl. Phys. **129**, 153101 (2021).

[54] F. Nafezarefi, S. Cornelius, J. Nijskens, H. Schreuders, and B. Dam, Effects of the addition of zirconium on the photochromic properties of yttrium oxy-hydride, Sol. Energy Mater. Sol. Cells **200**, 109923 (2019).

[55] G. Colombi, R. Stigter, D. Chaykina, S. Banerjee, A. P. M. Kentgens, S. W. H. Eijt, B. Dam, and G. A. de Wijs, Energy, metastability, and optical properties of anion-disordered REO_xH_{3-2x} (RE = Y, La) oxyhydrides: a computational study, Phys. Rev. B **105**, 054208 (2022).

[56] M. A. van Huis, A. van Veen, H. Schut, C. V. Falub, S. W. H. Eijt, P. E. Mijnarends, and J. Kuriplach, Positron confinement in embedded lithium nanoclusters, Phys. Rev. B **65**, 085416 (2002).

[57] A. Dupasquier and A. Mills Jr., *Positron Spectroscopy of Solids* (IOS Press, Amsterdam, 1995), Vol. 125.

[58] K. K. Ng, F. C. Zhang, V. I. Anisimov, and T. M. Rice, Electronic Structure of Lanthanum Hydrides with Switchable Optical Properties, Phys. Rev. Lett. **78**, 1311 (1997).

[59] J. J. Shi, Y. M. Li, Y. S. Li, D. M. Li, Y. H. Luo, H. J. Wu, and Q. B. Meng, From ultrafast to ultraslow: charge-carrier dynamics of perovskite solar cells, Joule **2**, 879 (2018).

[60] N. W. Ashcroft and N. D. Mermin, *Solid State Physics* (Holt, Rinehart and Winston, New York, 1976).

[61] A. Zangwill, *Modern Electrodynamics* (Cambridge University Press, Cambridge, 2013).

[62] H. C. van de Hulst, *Light Scattering by Small Particles* (Dover Publ., London, 1981).

[63] S. A. Maier, *Plasmonics: Fundamentals and Applications* (Springer, New York, 2007).

Correction: The byline footnote for the first author was missing and has been inserted.